

Magnon dark modes and gradient memory

Xufeng Zhang,^{1,*} Chang-Ling Zou,^{1,2,3,*} Na Zhu,¹ Florian Marquardt,^{4,5} Liang Jiang,² and Hong X. Tang¹

¹*Department of Electrical Engineering, Yale University, New Haven, Connecticut 06511, USA*

²*Department of Applied Physics, Yale University, New Haven, Connecticut 06511, USA*

³*Key Lab of Quantum Information, University of Science and Technology of China, CAS, Hefei, Anhui, 230026, China*

⁴*Institute for Theoretical Physics II, University of Erlangen-Nuremberg Staudtstr. 7, 91058 Erlangen, Germany*

⁵*Max Planck Institute for the Science of Light, Günther-Scharowsky-Straße 1/Bau 24, 91058 Erlangen, Germany*

Extensive efforts have been expended in developing hybrid quantum systems to overcome the short coherence time of superconducting circuits by introducing the naturally long-lived spin degree of freedom. Among all the possible materials, single-crystal yttrium iron garnet has shown up very recently as a promising candidate for hybrid systems, and various highly coherent interactions, including strong and even ultra-strong coupling, have been demonstrated. One distinct advantage of these systems is that the spins are in the form of well-defined magnon modes, which allows flexible and precise tuning. Here we demonstrate that by dissipation engineering, a non-Markovian interaction dynamics between the magnon and the microwave cavity photon can be achieved. Such a process enables us to build a magnon gradient memory to store information in the magnon dark modes, which decouple from the microwave cavity and thus preserve a long lifetime. Our findings provide a promising approach for developing long-lifetime, multimode quantum memories.

Hybrid systems provide a promising solution for coherent information storage by combining the long coherence time of spin ensembles with the power of superconducting circuits [1, 2]. Researches utilizing ensembles ranging from cold atomic gases [3] and magnetic molecules [4] to rare-earth-ion-doped crystals [5–7] and negatively-charged nitrogen vacancy (NV⁻) centres in diamond [8–12] have been reported recently. But not until very recently did people start to investigate the possibility of hybridizing yttrium iron garnet (YIG, Y₃Fe₅O₁₂), a ferrimagnetic insulator, with microwave cavities. In the YIG crystal, the coherent photon-spin ensemble interaction is greatly enhanced by the high spin density and can even approach the ultrastrong coupling regime [13–15]. Compared with previous dilute spin ensemble systems, direct spin-spin interaction leads to collective magnon excitations that have a range of distinct advantages, such as low damping rate, uniform distribution, rich nonlinear dynamics, and well-defined mode profiles and wave-vectors. Particularly, each piece of YIG can be treated as a giant spin, with the flexibility to be individually manipulated

in experiments.

In this work, we strongly couple multiple magnon modes with a microwave cavity resonance by placing multiple YIG spheres into a three dimensional (3D) cavity. With these coherently coupled magnons, collective effects [16] such as a magnon dark mode (subradiant mode) that is decoupled from the environment, as well as enhanced interaction between a magnon bright mode (superradiant mode) and a microwave mode are demonstrated. The spectrum of the magnons can be further adjusted by controlling the local magnetic field of each YIG sphere, which allows us to engineer the dissipation and tailor the dynamics of the microwave photon at will. With this method, we applied a magnetic field gradient, which induced the periodic evolution of the magnons between their temporal dark and bright modes, leading to a non-Markovian dynamics of the cavity energy that shows non-exponential decay and revival [17]. By optimizing the coupling condition [18], good efficiency is obtained and our theory analysis indicates that a unity efficiency is achievable. Our experiment is performed at room temperature, demonstrating the coherent, long-lifetime, broadband and multimode gradient memory effect. Since the principle is entirely based on linear interactions, such a magnon memory can be readily scaled down to the quantum regime at millikelvin temperatures, providing a new approach besides the existing schemes for dilute spin ensembles [19–26]. This allows the realization of hybrid quantum memories that do not suffer from common problems such as inhomogeneous broadening and so on.

As a general situation, consider N identical YIG spheres loaded in a copper microwave cavity. The linear coupling between the uniform magnon modes in the YIG spheres and the cavity TE₁₁₀ mode can be described by the Hamiltonian

$$\hat{\mathcal{H}}/\hbar = \omega_a \hat{a}^\dagger \hat{a} + \sum_{j=1}^N (\omega_j \hat{m}_j^\dagger \hat{m}_j + g_j \hat{a}^\dagger \hat{m}_j + g_j^* \hat{a} \hat{m}_j^\dagger), \quad (1)$$

where \hat{a} , \hat{m}_j are the bosonic operators associated with the photon and the uniform magnon modes, respectively, g_j is the coupling strength between the microwave mode and the magnon mode in the j -th YIG sphere with j ranging from 1 to N being the sphere index, ω_a is the resonance frequency of the TE₁₁₀ mode of the copper cavity with the YIG spheres loaded but at zero bias field, $\omega_j = \omega_a + [j - (N + 1)/2]\Delta\omega_m$ are the evenly distributed magnon resonance frequencies, and $\Delta\omega_m$ is

*These authors contributed equally to this work.

their frequency interval. Such a frequency distribution is obtained by biasing each YIG sphere at a magnetic field $H_j = H_0 + [j - (N + 1)/2]\Delta H$, where $H_0 = \omega_a/\gamma$ is the common external magnetic field that brings a YIG sphere on resonance with the microwave cavity TE₁₁₀ mode, $\gamma/2\pi = 2.8$ MHz/Oe is the gyromagnetic ratio, and $\Delta H = \Delta\omega_m/\gamma$ is the magnetic field difference between neighboring YIG spheres that is provided by the fine tuning of the small coils underneath each individual YIG sphere (Fig. 1a).

We first study the coherence of a simple system with two YIG spheres ($N = 2$). As a result of the mode hybridization for nonzero $g_{1,2}$, there exist three resonances in the cavity reflection spectrum when the two magnon modes are near resonance with the cavity TE₁₁₀ mode but not on resonance, which agrees well with our experimental observation (Fig. 1c). By fixing ΔH and sweeping the external magnetic field around H_0 , two avoided crossings are observed in the reflection spectra (Fig. 1d), indicating the strong coupling between the cavity mode and the two magnon modes. When the frequencies of the two magnon modes ($\omega_{1,2}$) are brought closer by tuning ΔH , the absorption of the middle resonance becomes weaker, which eventually vanishes in the spectrum when the two magnon modes are brought simultaneously on resonance with the cavity mode ($\omega_1 = \omega_2 = \omega_a$) by turning off the gradient ($\Delta H = 0$), and such a transition is evident in Figs. 1c-h. The remaining two resonances emerge from the hybridization of the bright (superradiant) magnon mode with the cavity photon mode, while the resonance that has disappeared from the spectrum is the dark (subradiant) magnon mode, as it decouples from the microwave cavity.

The concepts of the bright and dark modes are illustrated schematically in Fig. 1b. When the detuning field $\Delta H = 0$, the two magnon modes are on resonance $\omega_1 = \omega_2$. Since, in addition, we have $g_1 = g_2$, the bright mode is the superposition of the two magnon modes that precess in phase $\hat{B} = \frac{1}{\sqrt{2}}(\hat{m}_1 + \hat{m}_2)$, while the dark mode is the superposition of the two magnon modes that precess out of phase $\hat{D} = \frac{1}{\sqrt{2}}(\hat{m}_1 - \hat{m}_2)$. For the bright mode, the coherent interactions between the magnons and photons are collectively enhanced, leading to an enhanced coupling strength $g_B = \sqrt{2}g_{1,2}$, which is verified in the avoided crossing spectrum where the splitting for $\Delta H = 0$ ($2g/2\pi = 18.88$ MHz, Fig. 1f) is $\sqrt{2}$ times larger than that for $\Delta H = \pm 14$ Oe ($2g/2\pi = 13.42$ MHz, Figs. 1d&h). For the dark mode, the coupling of the two magnon modes with the cavity photons cancel each other, resulting in a vanishing coupling strength $g_D = 0$.

While the magnon bright mode can be used for information conversion with microwave photons, the dark mode is an ideal candidate for information storage because it decouples from the cavity and therefore has a very long lifetime [27]. A dark mode memory can be constructed if fast conversion between the bright and the dark mode is available, which in principle can be realized by rapidly tuning the magnetic bias field. However,

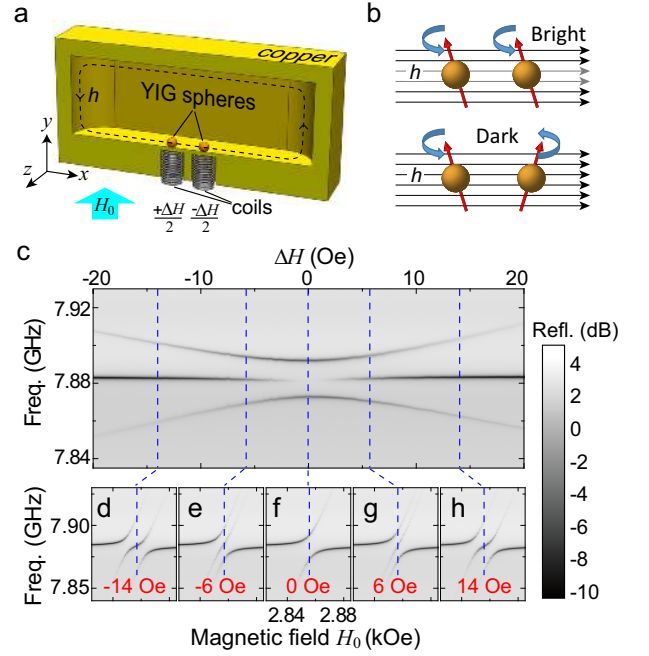


FIG. 1: **Magnon dark mode of two YIG spheres.** **a**, Device schematic including half of the copper cavity, two YIG spheres, and two small coils. H_0 : external bias magnetic field; ΔH : magnetic field gradient generated by the small coils; h : magnetic field of the microwave resonance (TE₁₁₀ mode) in the copper cavity. **b**, Conceptual illustration of the magnon bright and dark modes: the bright mode is coupled to while the dark mode is isolated from the microwave magnetic field h . **c**, Reflection spectra as a function of ΔH under an external bias magnetic field $H_0 = 2858$ Oe. **d-h**, Reflection spectra as a function of bias magnetic field H_0 at a fixed magnetic field gradient $\Delta H = -14, -6, 0, 6, 14$ Oe, respectively. Each dashed line in **c** corresponds to the dashed line in each of the spectral maps in **d-h**.

the slow response of the local inductive coils prohibits the experimental realization of such an approach. Alternatively, we consider here a magnon gradient memory (MGM) using magnon *temporal dark modes* which eliminates the need of fast magnetic control. Such temporal dark modes are created by applying a magnetic field gradient ($\Delta H \neq 0$) to uniformly detune the magnon modes around the cavity resonance, so unlike the steady bright and dark modes discussed above, they are not the eigenmodes of the Hamiltonian. Instead, the non-Markovian dynamics of such a coupled system leads to a temporally evolving inter-conversion between the temporal bright and dark modes, which provides a good solution for fast memory operations without adding extra controls.

For a device consisting of N YIG spheres, a frequency spectrum with $N + 1$ resonances spaced at an interval of $\Delta\omega$ ($\approx \Delta\omega_m$ for large N) can be obtained as a result of the coupling between the cavity mode and the uniformly distributed magnon modes. To achieve a memory with high efficiency, it is also important to ensure uniform coupling strengths for all the YIG spheres ($g_j = g_0$, see

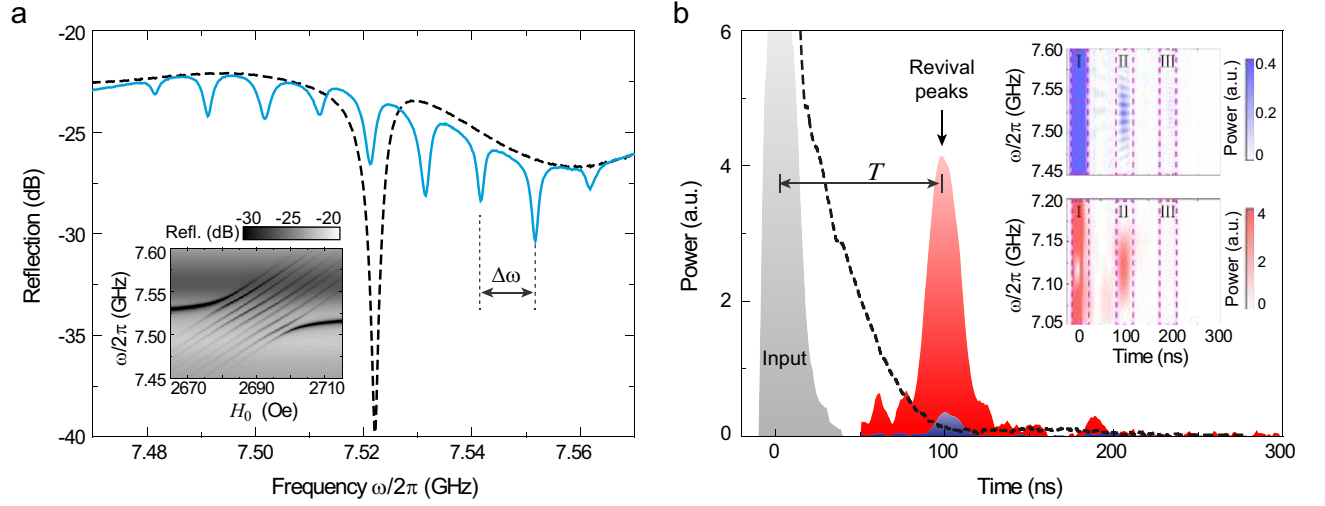


FIG. 2: **The magnon gradient memory.** **a**, Reflection spectra of the microwave cavity with eight YIG spheres at a bias field (H_0) of 2687 Oe (solid blue line) and 0 Oe (dashed black line), respectively. The frequency gradient of the magnon modes is tuned to be $\Delta\omega = 2\pi \times 10$ MHz. Inset: the reflection frequency spectra of the MGM at various bias magnetic fields. **b**, The dynamics of the MGM output for a 15 ns pulsed microwave excitation (gray) at the under-coupling (blue) and critical-coupling (red) conditions with a frequency gradient of $\Delta\omega = 2\pi \times 10$ MHz. Dashed black curve shows the exponential decay when the magnons are largely detuned. Operation condition for the blue curve: $\omega = 2\pi \times 7.522$ GHz, $H_0 = 2687$ Oe; black: $\omega = 2\pi \times 7.522$ GHz, $H_0 = 0$ Oe; red: $\omega = 2\pi \times 7.120$ GHz, $H_0 = 2544$ Oe. The input frequency for each case is adjusted accordingly with the cavity resonance shift induced by the change of the external coupling. Inset: pulse retrieval at various frequencies for the under-coupling (top) and critical-coupling (bottom) condition, respectively. Zone I: reflection at the time of input due to the under-coupling condition of the external coupling; Zone II: first revival peaks; Zone III: second revival peaks.

Supplementary Information for details). The collective magnon modes from the N YIG spheres can be expressed as one temporal bright mode, expressed as

$$\hat{B} = \frac{1}{\sqrt{N}} \sum_{j=1}^N \hat{m}_j, \quad (2)$$

and $N-1$ temporal dark modes, with the n -th dark mode expressed as

$$\hat{D}_n = \frac{1}{\sqrt{N}} \sum_{j=1}^N \hat{m}_j e^{2\pi i(j - \frac{N+1}{2}) \cdot n/N}, \quad (3)$$

which do not couple to the cavity. Due to the uniformly-spaced detuning, the magnon modes described by Eqs. (2) and (3) will convert from one to another with a time interval T/N , where $T = 2\pi/\Delta\omega$ is the evolution period of the collective magnon modes. During the storing process, the cavity photons are first converted to the temporal bright magnon mode, which is then successively converted to the temporal dark magnon modes that prevent the radiation loss. After one period, the system evolves back to the bright mode, and the information retrieves from the magnons and converts back to microwave photons. Both storing and retrieving processes are accelerated due to the superradiance effect. In such a configuration, no external control, such as refocusing pulse or gradient inversion, is required to retrieve the

stored information. The performance of such an MGM depends on the number of YIG spheres. A larger N helps to improve the pulse re-construction and suppress the off-peak ripples (Supplementary Information).

In our experiments, we demonstrate such an MGM using eight YIG spheres ($N = 8$). The large tunability of the magnon allows us to engineer the cavity dissipation with great flexibility and obtain a reflection spectrum with a total of $N+1 = 9$ uniformly distributed hybrid modes, as shown in Fig. 2a (solid blue line), where $\Delta\omega/2\pi = 10$ MHz. Note that, in contrast to the stationary dark mode, the temporal dark modes can be detected in the spectrum since they convert back to the bright mode periodically. In other words, each of the 9 resonance lines in the steady state spectrum contains some component from the temporal bright mode which can be detected. When a 15-ns-long pulsed microwave signal at a frequency $\omega = \omega_a = 7.52$ GHz is injected into the cavity with an external bias magnetic field of 2687 Oe, it couples to the magnon bright mode and then converts to the magnon dark modes. The retrieval of the stored pulse takes place after a pre-programmed time $T = 2\pi/\Delta\omega = 100$ ns (blue peak in Fig. 2b), in sharp contrast with the exponential decay when the magnons are strongly detuned by turning off the external bias magnetic field H_0 (dashed black line in Fig. 2b). While the MGM works without the requirement of any time-dependent control, extensions of the scheme would be possible when that control becomes available. For in-

stance, on-demand recall can be achieved via dynamic control by rapidly turning off and on the magnetic field gradient. Moreover, further dissipation engineering by controlling the field gradient would allow even more complicated manipulation of the output pulses, such as sequence reversal, pulse splitting, and so on. However, a fast magnetic field tuning at this time scale with reasonably large amplitude (around 50 Oe) is difficult to achieve and so it falls beyond the scope of this work and is left for future study.

The performance of the MGM can be significantly improved by optimizing the external coupling condition. Blue curves in Figs. 2a & b correspond to the condition of under-coupling and therefore the retrieved pulse is very weak. A drastic boost of the revival pulse is obtained (red peak in Fig. 2b) by adjusting the coaxial probe to meet the critical coupling (impedance matching) condition: $\kappa_{a,1} = \kappa_{a,0} + \pi|g|^2/\Delta\omega$, where $\kappa_{a,0}$ is the amplitude damping rate of the cavity resonance and $\kappa_{a,1}$ is the coupling rate from the coaxial probe. The critical coupling condition allows a complete energy conversion into the magnon bright mode (see Supplementary Information), and it also results in a maximized signal retrieval back to the microwave photon. Therefore, the first revival peak will contain all the stored information and there will be no successive revival peaks as observed in the under-coupling situation. Such analysis matches our measurement results shown in the insets of Fig. 2b: the second revival peaks (zone III) are relatively strong compared with the first revival peaks (zone II) for the under-coupling situation (top inset), while for the critical-coupling situation (bottom inset) the second revival peaks disappear.

One advantage of the MGM is that its operation is not restricted to a narrow frequency range. A uniform frequency distribution exists in a wide frequency range as we vary the bias magnetic field (Fig. 2a, inset). Accordingly, broad-band pulse retrieval process can be obtained in the time-domain measurement. Generally, the operation bandwidth can be determined by $N\Delta\omega$, and therefore, the delay-bandwidth product is set by N . In the experiment, we observed retrieval peaks in a broad frequency band of 80 MHz at a bias magnetic field of 2687 Oe (Fig. 2b, insets), which is 1-2 orders of magnitude larger than the linewidth of the photon or magnon resonances. Note that when sweeping the input frequency, the revival peak intensity periodically varies for the under-coupling situation (Fig. 2b, top inset, zone II), which can be attributed to the periodic variation in the coupling condition, while such a phenomenon disappears in the critically coupled situation thanks to the improved coupling condition.

We quantitatively characterized the MGM by measuring the delay time and the retrieval efficiency as a function of $\Delta\omega$, and the result is plotted in Fig. 3a. As $\Delta\omega$ reduces, the revival time T increases, and the measurement results perfectly follow the relation $T = 2\pi/\Delta\omega$ (Fig. 3b). The MGM retrieval efficiency is defined as the ratio of the output pulse energy to the input pulse energy. It has

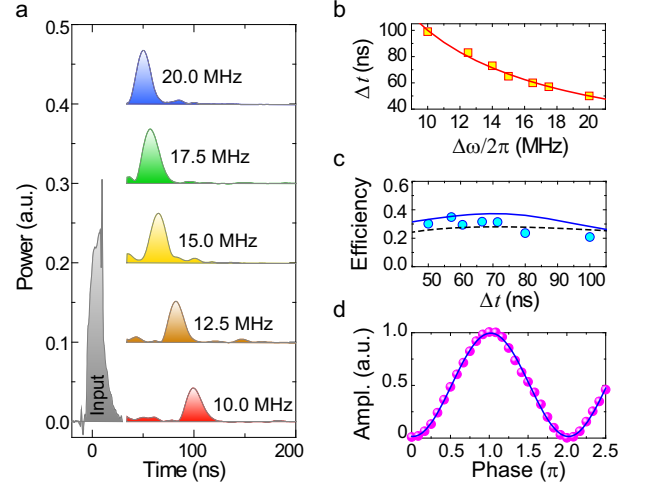


FIG. 3: Characterization of magnon gradient memory. **a**, Measured retrieval pulses for different frequency gradients $\Delta\omega/2\pi$. The input pulse is only shown for $\Delta\omega/2\pi = 10$ MHz and remains the same for the other cases. **b**, Extracted storage time as a function of frequency gradient. The solid line is calculated by $T = 2\pi/\Delta\omega$. **c**, Retrieval efficiency as a function of the storage time obtained from the measurement (circles), the numerical fitting (solid blue line), and the calculation using Eq. (4) (dashed black line), respectively. **d**, Measured interference between the retrieved and reference signals as a function of their phase difference. The solid line is a sinusoidal fitting.

been extracted as a function of delay time and plotted in Fig. 3c (blue circles), showing an efficiency of about 30% under the critical coupling condition. The extracted efficiencies match the numerical simulation results obtained using the same parameters as in the measurement (solid blue line). On the other hand, the efficiency can be approximated using the asymptotic expression (see Supplementary Information)

$$\zeta \approx e^{-2\pi/F} \left[1 - \frac{1}{t_p \kappa_{a,0} (1 + G)} \right] \left(\frac{G}{1 + G} \right)^2, \quad (4)$$

which is plotted in Fig. 3c (dashed black) for comparison. Equation (4) shows that the MGM efficiency depends on the figure of merit $G = \frac{\pi C}{2F}$ for an input pulse with a duration of t_p , where $F = \frac{\Delta\omega}{2\kappa_m}$ is the finesse of the magnon gradient and $C = \frac{|g|^2}{\kappa_m \kappa_{a,0}}$ is the magnon-photon interaction cooperativity. Here we assume all the magnon modes in each YIG sphere have the same amplitude damping rate (κ_m). Therefore by optimizing C and F we can further improve the MGM performance. In practice, F can be well controlled to be in the range of $10^1 - 10^2$, and C in the order of $10^2 - 10^4$, and thus $\zeta \approx 1$ is achievable for real applications.

In addition to the high achievable efficiency, such an MGM preserves the signal coherence during the storage and retrieval process. Figure 3d plots the measured inter-

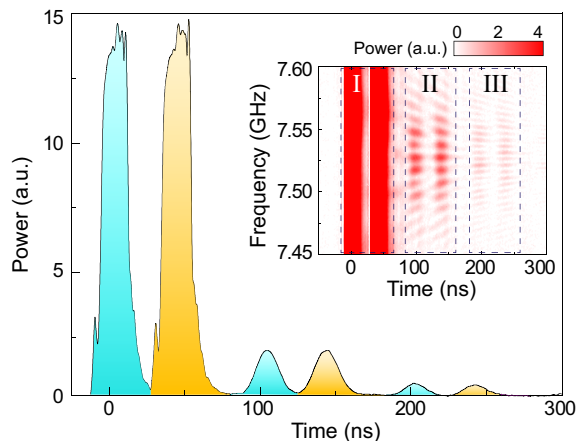


FIG. 4: **Multi-pulse storage in the MGM.** Retrieved pulses for a double-pulse excitation. The two pulses are separated by 40 ns with a 15 ns duration each. Inset: double-pulse retrieval for various input frequencies at a bias field of 2687 Oe.

ference signal between the retrieved pulse (after a 100-ns storage time) and the input microwave signal. The periodic dependence of the interferometer output on the relative phase between these two signals indicates they are still phase coherent. A visibility as high as $96.9 \pm 1.5\%$ can be extracted, proving the high coherence preservation feature of our MGM.

Another advantage of the MGM is its multimode operation capability, which is crucial for speeding up quantum computation protocols. Figure 4 plots the output of the MGM when two identical pulses are sent into the memory. The input pulses are 15 ns in duration and separated by 40 ns. Two pulses are retrieved from the memory after the pre-programmed storage time $T = 100$ ns. As there is no echo process involved during the memory process, the MGM operates in a first-in-first-out (FIFO) mode. The multimode operation can be also achieved in a wide frequency range (Fig. 4, inset). The occasional pulse distortion at certain frequencies is a result of the non-ideality of the system such as the non-identical coupling strengths and decay rates of different YIG spheres, or the impact of the high order magnon modes.

In summary, we demonstrated coherent coupling of multimode magnon resonances to a single microwave cavity. The dark magnon mode of two YIG spheres is observed. We used the temporal magnon dark mode to establish non-Markovian dynamics in a system consisting of eight YIG spheres, and showed its potential in developing quantum memories, which are broadband, multimode, and do not require fast field switching. Our investigation on a novel mechanism of manipulating magnons

and microwave photons paves the route towards magnon-based hybrid quantum memories, quantum repeaters as well as quantum networks [28].

Methods

Sample preparation. The microwave cavities are machined from high-conductivity copper. The cavity housing two YIG spheres has a dimension of $43 \times 21 \times 9.6$ mm³, with its TE₁₁₀ resonating at 7.87 GHz, while the one housing eight YIG spheres has a dimension of $50 \times 21 \times 4.8$ mm³, with its TE₁₁₀ mode resonating at 7.52 GHz. All the YIG spheres are highly polished and have a diameter of 0.25 mm, with their $\langle 110 \rangle$ direction aligned parallel to the external bias magnetic field. The mounting ceramic rods that hold the YIG spheres are glued on the cavity wall, close to the the maximum magnetic field of the cavity resonance to achieve strong magnon-photon coupling. Eight holes, 6.5 mm apart from each other, are drilled deep into (but not through) the cavity wall underneath the YIG spheres, where eight home-made small coils (200 turns, 6 mm in diameter, made of 32-gauge copper wires) are inserted with a 1 mm distance from the YIG spheres for fine tuning of the bias magnetic fields within a range of ± 30 Oe (Figs. 1a & S5a). The whole device assembly is inserted between the two poles of a water-cooled electromagnet which provides the strong external bias magnetic field.

Microwave characterization. The frequency spectra are taken using a vector network analyzer by measuring the reflection signal from the coaxial probe which accesses the cavity mode through a small hole in the cavity wall. The external coupling can be tuned by adjusting the position of the coaxial probe. The time traces are measured using a high-speed oscilloscope when the continuous-wave (CW) input microwave signal is modulated by a pulse generator through a transistor-transistor logic (TTL) switch which gives a rectangular pulse shape. To measure the coherence between the retrieved pulse and the input signal, the CW input signal is split into two branches before the pulse modulation, one of which, serving as the reference, is phase adjusted and combined with the retrieved signal before sending into an envelope detector. Then, the visibility of interference between the retrieved signal and the reference is measured by varying the reference phase. More details about the microwave characterization can be found in the Supplementary Information.

Theoretical derivation. In the Supplementary Information, details about the theory derivation and analysis of the dark mode and the gradient memory are provided.

[1] Wallquist, M., Hammerer, K., Rabl, P., Lukin, M. & Zoller, P. Hybrid quantum devices and quantum engi-

neering. *Phys. Scr.* **T137**, 014001 (2009).

[2] Xiang, Z.-L., Ashhab, S., You, J. & Nori, F. Hybrid

- quantum circuits: superconducting circuits interacting with other quantum systems. *Rev. Mod. Phys.* **85**, 623–653 (2013).
- [3] Verdú, J. *et al.* Strong magnetic coupling of an ultracold gas to a superconducting waveguide cavity. *Phys. Rev. Lett.* **103**, 043603 (2009).
 - [4] Eddins, A. W., Beedle, C. C., Hendrickson, D. N. & Friedman, J. R. Collective coupling of a macroscopic number of single-molecule magnets with a microwave cavity mode. *Phys. Rev. Lett.* **112**, 120501 (2014).
 - [5] Schuster, D. I. *et al.* High-cooperativity coupling of electron-spin ensembles to superconducting cavities. *Phys. Rev. Lett.* **105**, 140501 (2010).
 - [6] Probst, S. *et al.* Anisotropic rare-earth spin ensemble strongly coupled to a superconducting resonator. *Phys. Rev. Lett.* **110**, 157001 (2013).
 - [7] Tkalcic, A. *et al.* Strong coupling of an Er^{3+} -doped YAlO_3 crystal to a superconducting resonator. *Phys. Rev. B* **90**, 075112 (2014).
 - [8] Zhu, X. *et al.* Coherent coupling of a superconducting flux qubit to an electron spin ensemble in diamond. *Nature* **478**, 221–224 (2011).
 - [9] Kubo, Y. *et al.* Hybrid quantum circuit with a superconducting qubit coupled to a spin ensemble. *Phys. Rev. Lett.* **107**, 220501 (2011).
 - [10] Amsüss, R. *et al.* Cavity QED with magnetically coupled collective spin states. *Phys. Rev. Lett.* **107**, 060502 (2011).
 - [11] Marcos, D. *et al.* Coupling nitrogen-vacancy centers in diamond to superconducting flux qubits. *Phys. Rev. Lett.* **105**, 210501 (2010).
 - [12] Ranjan, V. *et al.* Probing dynamics of an electron-spin ensemble via a superconducting resonator. *Phys. Rev. Lett.* **110**, 067004 (2013).
 - [13] Huebl, H. *et al.* High cooperativity in coupled microwave resonator ferrimagnetic insulator hybrids. *Phys. Rev. Lett.* **111**, 127003 (2013).
 - [14] Zhang, X., Zou, C.-L., Jiang, L. & Tang, H. X. Strongly coupled magnons and cavity microwave photons. *Phys. Rev. Lett.* **113**, 156401 (2014).
 - [15] Tabuchi, Y. *et al.* Hybridizing ferromagnetic magnons and microwave photons in the quantum limit. *Phys. Rev. Lett.* **113**, 083603 (2014).
 - [16] Dicke, R. Coherence in spontaneous radiation processes. *Phys. Rev.* **93**, 99–110 (1954).
 - [17] Zou, C.-L. *et al.* Photonic simulation of system-environment interaction: non-Markovian processes and dynamical decoupling. *Phys. Rev. A* **88**, 063806 (2013).
 - [18] Afzelius, M. & Simon, C. Impedance-matched cavity quantum memory. *Phys. Rev. A* **82**, 022310 (2010).
 - [19] Hau, L. V., Harris, S. E., Dutton, Z. & Behroozi, C. H. Light speed reduction to 17 metres per second in an ultracold atomic gas. *Nature* **397**, 594–598 (1999).
 - [20] Anderson, A. *et al.* Spin echo serial storage memory. *J. Appl. Phys.* **26**, 1324–1338 (1955).
 - [21] Alexander, A. L., Longdell, J. J., Sellars, M. J. & Manson, N. B. Photon echoes produced by switching electric fields. *Phys. Rev. Lett.* **96**, 043602 (2006).
 - [22] Hosseini, M., Sparkes, B. M., Campbell, G., Lam, P. K. & Buchler, B. C. High efficiency coherent optical memory with warm rubidium vapour. *Nat. Commun.* **2**, 174 (2011).
 - [23] Hedges, M. P., Longdell, J. J., Li, Y. & Sellars, M. J. Efficient quantum memory for light. *Nature* **465**, 1052–1056 (2010).
 - [24] Kraus, B. *et al.* Quantum memory for nonstationary light fields based on controlled reversible inhomogeneous broadening. *Phys. Rev. A* **73**, 020302 (2006).
 - [25] Arnold, S., Whitten, W. B., Ramsey, J. M. & Liu, C. T. Room-temperature microparticle-based persistent spectral hole burning memory. *Opt. Lett.* **16**, 420–422 (1991).
 - [26] de Riedmatten, H., Afzelius, M., Staudt, M. U., Simon, C. & Gisin, N. A solid-state light-matter interface at the single-photon level. *Nature* **456**, 773–777 (2008).
 - [27] Dong, C., Fiore, V., Kuzyk, M. C. & Wang, H. Optomechanical dark mode. *Science* **338**, 1609–1613 (2012).
 - [28] Kimble, H. J. The quantum internet. *Nature* **453**, 1023–1030 (2008).

Acknowledgments

This work is supported by DARPA/MTO MESO program. H.X.T. acknowledges support from a Packard Fellowship in Science and Engineering. L.J. acknowledges support from the Alfred P. Sloan Foundation, the Packard Foundation, the Multidisciplinary University Research Initiative (MURI), and the DARPA Quiness program. C.L.Z. acknowledges National Basic Research Program of China (Grant Nos. 2011CB921200 and 2011CBA00200). F.M. acknowledges ERC OPTOMECH and DARPA ORCHID. The authors thank Dr. Michel H. Devoret and Dr. Michael Hatridge for providing a prototype 3D microwave cavity.

Author contributions

X.Z. prepared the samples, performed the measurements and data analysis. C.L.Z. and L.J. conceived the idea. C.L.Z., L. J. and F.M. provided theoretical analysis. N.Z. assisted with the measurements. L.J. and H.X.T. supervised the project. X.Z., C.L.Z., F.M., L.J., and H.X.T. wrote the manuscript.

Additional information

Supplementary Information is available in the online version of the paper. Reprints and permissions information is available online at www.nature.com/reprints. Correspondence and requests for materials should be addressed to H.X.T. (hong.tang@yale.edu).

Competing financial interests

The authors declare no competing financial interests.

Supplementary Information

Contents

References	5
I. Microwave photon-magnon strong coupling	S1
II. Reflection spectrum	S1
III. Dark magnon modes	S2
A. Two Magnon Modes	S2
B. Generalization to Multiple Magnon Modes	S2
C. Temporal Dark Magnon Mode	S3
IV. Magnon gradient memory	S3
A. Intuitive Explanation	S3
B. Dynamics	S4
C. Asymptotic Solution	S4
D. Scattering Picture	S5
E. Critical coupling condition	S6
F. Photon Retrieval	S7
G. Measurement Scheme	S8
H. Experimental Imperfections	S8

I. MICROWAVE PHOTON-MAGNON STRONG COUPLING

The interaction between microwave photon and magnon (single mode) can be described by the Hamiltonian with the rotating-wave approximation

$$\hat{\mathcal{H}}/\hbar = \omega_a \hat{a}^\dagger \hat{a} + \omega_m \hat{m}^\dagger \hat{m} + g(\hat{a}^\dagger \hat{m} + \hat{a} \hat{m}^\dagger), \quad (\text{S1})$$

where \hat{a}^\dagger (\hat{a}) is the creation (annihilation) operator for the microwave photon at frequency ω_a . For the uniform magnon mode, the collective spin excitations are approximately represented by the Boson operator \hat{m}^\dagger (\hat{m}) with Holstein-Primakoff approximation [S1] and ω_m is the magnon frequency. The coupling strength g between the two systems is [S2]:

$$g = \frac{\eta}{2} \gamma \sqrt{\frac{\hbar \omega \mu_0}{V_a}} \sqrt{2Ns}, \quad (\text{S2})$$

where ω is the resonance frequency, γ is the gyromagnetic ratio, V_a is the modal volume of the microwave cavity resonance, μ_0 is the vacuum permeability, N is the total number of spins, and $s = \frac{5}{2}$ is the spin number of the ground state Fe^{3+} ion in YIG. The coefficient $\eta \leq 1$ describes the spatial overlap and polarization matching conditions between the microwave field and the magnon mode, which can be explicitly written as:

$$\eta^2 = \frac{(\vec{h}(\mathbf{r}) \cdot \vec{e}_x)^2 + (\vec{h}(\mathbf{r}) \cdot \vec{e}_y)^2}{\max\{|\vec{h}(\mathbf{r})|^2\}}, \quad (\text{S3})$$

where $\max\{|\vec{h}(\mathbf{r})|^2\}$ is the maximum magnetic field intensity of the cavity mode, and $\vec{h}(\mathbf{r})$ is the magnetic field amplitude at the location (\mathbf{r}) of the YIG sphere, \vec{e}_j with $j = x, y, z$ are unit vectors and \vec{e}_z is along the bias field direction.

II. REFLECTION SPECTRUM

In our experiment, we measure the reflection spectrum under continues driving and the emission after pulsed excitations of the microwave cavity, which correspond to the eigenmode spectrum and the transient cavity output, respectively. In general, the equation of motion for the cavity photon is

$$\frac{d}{dt} \hat{a} = -i[\hat{a}, \hat{\mathcal{H}}] - i\sqrt{2\kappa_{a,1}} E_{\text{in}}(t) e^{-i\omega_l t}, \quad (\text{S4})$$

where $\hat{\mathcal{H}}$ is the system Hamiltonian, $\kappa_{a,1}$ is the cavity external coupling rate to the coaxial probe, $E_{\text{in}}(t)$ and ω_l are the amplitude and frequency of the input microwave.

In the rotating frame of ω_l , the microwave electric field collected by the detector reads

$$E_{\text{out}}(t) = -E_{\text{in}}(t) + i\sqrt{2\kappa_{a,1}} \hat{a}(t) \quad (\text{S5})$$

For a continuous stable input $E_{\text{in}}(t) = E_{\text{in}}$, we measure the stationary spectra with the normalized spectrum expressed as

$$r(\omega_l) = -1 + i\sqrt{2\kappa_{a,1}} \frac{\hat{a}(\omega_l)}{E_{\text{in}}}. \quad (\text{S6})$$

For the memory operation, the retrieval of the microwave pulse is measured after the input pulse is stored, and the detected intensity is

$$I(t) = 2\kappa_{a,1} |\langle \hat{a}(t) \rangle|^2. \quad (\text{S7})$$

The efficiency of the MGM, defined as the energy ratio of the retrieval pulse to the input pulse, can be expressed as

$$\zeta = \frac{\int I(t) dt}{\int I_{\text{in}}(t) dt}. \quad (\text{S8})$$

[S1] Holstein, T. and Primakoff, H. *Phys. Rev.* **58**, 1098 (1940).

[S2] Zhang, X., Zou, C.-L., Jiang, L., and Tang, H. X. *Phys. Rev. Lett.* **113**, 156401 (2014).

III. DARK MAGNON MODES

In general, the Hamiltonian of multiple linearly coupled magnon modes and the cavity mode reads:

$$\hat{\mathcal{H}}/\hbar = \omega_a \hat{a}^\dagger \hat{a} + \sum_{j=1}^N (\omega_j \hat{m}_j^\dagger \hat{m}_j + g_j \hat{a}^\dagger \hat{m}_j + g_j^* \hat{a} \hat{m}_j^\dagger). \quad (\text{S9})$$

When deriving the equations of motion, both the magnon dissipation and the cavity dissipation (including the external coupling) are considered. In principle, the input-output theory shows that this gives a damping term as well as a fluctuation (including vacuum and thermal) term. To keep the notation simple, we will, from now on, use symbols like a and m_j to refer to the expectation values of the underlying operators. Therefore, the fluctuation terms will be dropped. This is sufficient to obtain the linear scattering behavior of the system and to discuss its eigenmodes. With this proviso, the equations of motion for the cavity mode and the magnon modes are:

$$\frac{d}{dt}a = (-i\omega_a - \kappa_a)a - i \sum_j g_j m_j, \quad (\text{S10})$$

$$\frac{d}{dt}m_j = (-i\omega_j - \kappa_j)m_j - i g_j^* a. \quad (\text{S11})$$

Here, κ_a and κ_j are the total decay rates of the cavity photon and the magnon modes, respectively, with κ_a including both the internal dissipation ($\kappa_{a,0}$) as well as the coupling to the coaxial probe ($\kappa_{a,1}$).

A. Two Magnon Modes

As described in the main text, we first study the case with two magnon modes. For simplicity, let the two magnon modes be on-resonance with the cavity mode ($\omega_1 = \omega_2 = \omega_m$). Then the dynamics of the cavity field is

$$\frac{d}{dt}a = (-i\omega_a - \kappa_a)a - i(g_1 m_1 + g_2 m_2). \quad (\text{S12})$$

The cavity mode couples to the collective mode $B = (g_1 m_1 + g_2 m_2)/\sqrt{|g_1|^2 + |g_2|^2}$ as

$$\frac{d}{dt}B = (-i\omega_m - \kappa_m)B - i\sqrt{|g_1|^2 + |g_2|^2}a. \quad (\text{S13})$$

And the orthogonal mode $D = (g_2^* m_1 - g_1^* m_2)/\sqrt{|g_1|^2 + |g_2|^2}$ satisfies

$$\frac{d}{dt}D = (-i\omega_m - \kappa_m)D - i(g_1^* g_2^* - g_2^* g_1^*)a/\sqrt{|g_1|^2 + |g_2|^2} \quad (\text{S14})$$

$$= (-i\omega_m - \kappa_m)D. \quad (\text{S15})$$

Therefore, D is completely isolated from the cavity mode, representing the dark mode that cannot be detected from the reflection spectrum of the microwave cavity.

B. Generalization to Multiple Magnon Modes

For multiple magnon modes $N \geq 2$ and $\omega_j = \omega_1$ for $j = 2, \dots, N$, the normalized bright mode is

$$B = \sum_{j=1}^N g_j m_j / \sqrt{\sum_{j=1}^N |g_j|^2}. \quad (\text{S16})$$

Then we have

$$\frac{d}{dt}a = (-i\omega_a - \kappa_a)a - i\sqrt{\sum_{j=1}^N |g_j|^2}B. \quad (\text{S17})$$

If the magnons are identical, the bright mode is a collective mode of all the magnon modes with the coupling strength being enhanced by a factor of

$$f = \sqrt{\sum_j |g_j|^2} / g_1 = \sqrt{N}. \quad (\text{S18})$$

There are $N - 1$ other modes, orthogonal to the bright mode and decoupled from the cavity.

C. Temporal Dark Magnon Mode

In the above analysis, all the magnon modes are on resonance with the cavity mode, and therefore the bright and dark modes are all the eigenmodes of the Hamiltonian. When the magnon modes are tuned off but close to resonance, situation would be different. As an example, we consider the case of two magnon modes. If the two magnon modes are detuned from the cavity mode as

$$\omega_1 = \omega_a + \Delta\omega/2, \quad (\text{S19})$$

$$\omega_2 = \omega_a - \Delta\omega/2, \quad (\text{S20})$$

then we can define the temporal bright mode at time t as (assuming $g_1 = g_2 = g_m$)

$$\tilde{B}(t) = \frac{1}{\sqrt{2}} e^{-i\omega_a t} \left(m_1 e^{-i\Delta\omega t/2} + m_2 e^{i\Delta\omega t/2} \right). \quad (\text{S21})$$

At $t = 0$, this mode is $B = \frac{1}{\sqrt{2}}(m_1 + m_2)$, which is the same as static bright mode discussed above. But at $t = \frac{\pi}{\Delta\omega}$, the mode evolves to

$$\tilde{B}\left(\frac{\pi}{\Delta\omega}\right) = \frac{-i}{\sqrt{2}} e^{-i\omega_a \pi/\Delta\omega} (m_1 - m_2) = -i e^{-i\omega_a \pi/\Delta\omega} D, \quad (\text{S22})$$

which is the dark mode that decouples from the cavity. Therefore, in this scenario, the temporal bright and dark magnon modes are not eigenmodes of the system and they are inter-convertible through time evolution.

IV. MAGNON GRADIENT MEMORY

A. Intuitive Explanation

To realize a magnon memory device using the temporal magnon dark mode, we want: (1) the input photon can be converted to the collective magnon bright mode as quickly as possible, and therefore the photon energy will not dissipate too much due to the cavity intrinsic loss; (2) the bright mode can convert to the dark mode once the input photon is converted to the bright mode; (3) the retrieval of the photon is predictable and pre-programmable.

To fulfill these requirements, the system should consist of multiple magnon modes with equal detuning. Assuming the lifetime of the magnon and the cavity photon are $\tau_m = 1/2\kappa_m$ and $\tau_a = 1/2\kappa_a$, respectively, the retrieval period $T = \pi/\Delta\omega$, the conversion time from the bright mode to the dark modes $t_{B \rightarrow D} = T/N$ with N being the total number of the magnon modes, and the conversion time from the cavity photon to the magnon bright mode $t_{a \rightarrow B} = \pi/\sqrt{N}g$, then we will have the following constraints

$$T \leq \tau_m, \quad (\text{S23})$$

$$t_{B \rightarrow D} \geq t_{a \rightarrow B}, \quad (\text{S24})$$

$$t_{a \rightarrow B} \ll \tau_a, \quad (\text{S25})$$

which can be rewritten as

$$\Delta\omega \geq \frac{\pi}{\tau_m} = 2\pi \times \kappa_m, \quad (\text{S26})$$

$$g \geq \sqrt{N}\Delta\omega \geq 2\pi\sqrt{N} \times \kappa_m, \quad (\text{S27})$$

$$g \gg \frac{2\pi}{\sqrt{N}} \times \kappa_{a,0}. \quad (\text{S28})$$

A highly efficient magnon gradient memory requires the cooperativity $C = \frac{g^2}{\kappa_{a,0}\kappa_m} \gg 4\pi^2$. In our experiment, the hybrid YIG sphere-3D cavity structure can have a cooperativity C as large as 10^4 , and therefore it is very promising for memory applications.

B. Dynamics

In an ideal magnon gradient memory, we have

$$\omega_j = \omega_a - \frac{N-1}{2}\Delta\omega + j\Delta\omega \quad (\text{S29})$$

for the uniform magnon mode in the j -th YIG sphere. Since

$$\frac{d}{dt}m_j = (-i\omega_j - \kappa_j)m_j - ig_j^*a, \quad (\text{S30})$$

we have the formal solution for the magnon time-evolution (where $m_j(0) = 0$):

$$m_j(t) = -ig_j^* \int_0^t a(\tau) e^{(-i\omega_j - \kappa_j)(t-\tau)} d\tau. \quad (\text{S31})$$

Then, the cavity dynamics is

$$\frac{d}{dt}a = (-i\omega_a - \kappa_a)a - \sum_j |g_j|^2 \int_0^t a(\tau) e^{(-i\omega_j - \kappa_j)(t-\tau)} d\tau \quad (\text{S32})$$

$$= (-i\omega_a - \kappa_a)a - \int_0^t a(\tau) \sum_j |g_j|^2 e^{(-i\omega_j - \kappa_j)(t-\tau)} d\tau. \quad (\text{S33})$$

For N identical YIG spheres with $g_j = g$ and $\kappa_j = \kappa_m$, we have

$$\begin{aligned} \sum_j |g_j|^2 e^{(-i\omega_j - \kappa_j)(t-\tau)} &= \sum_j |g_j|^2 e^{(-i\omega_a - i\frac{N-1}{2}\Delta\omega - ij\Delta\omega - \kappa_m)(t-\tau)} \\ &= |g|^2 e^{(-i\omega_a - i\frac{N-1}{2}\Delta\omega - \kappa_m)(t-\tau)} \sum_{j=1}^N e^{-ij\Delta\omega(t-\tau)} \\ &= |g|^2 e^{(-i\omega_a - \kappa_m)(t-\tau)} \frac{\sin[\frac{N\Delta\omega(t-\tau)}{2}]}{\sin[\frac{\Delta\omega(t-\tau)}{2}]}. \end{aligned} \quad (\text{S34})$$

Finally, the cavity dynamics is determined by the following equation

$$\frac{d}{dt}a(t) = (-i\omega_a - \kappa_a)a(t) - |g|^2 \int_0^t a(\tau) e^{(-i\omega_a - \kappa_m)(t-\tau)} \frac{\sin[\frac{N\Delta\omega(t-\tau)}{2}]}{\sin[\frac{\Delta\omega(t-\tau)}{2}]} d\tau. \quad (\text{S35})$$

C. Asymptotic Solution

As shown by Fig. S1, we can take the approximation

$$\frac{\sin[\frac{N\Delta\omega(t-\tau)}{2}]}{\sin[\frac{\Delta\omega(t-\tau)}{2}]} \approx 2\pi \sum_l (-1)^{l(N-1)} \delta[\Delta\omega(t-\tau - l\frac{2\pi}{\Delta\omega})] \quad (\text{S36})$$

for $N \gg 1$, where $\delta(x)$ is the Dirac delta function.

Therefore, we can describe the cavity dynamics for $N \gg 1$ as

$$\begin{aligned} \frac{d}{dt}a(t) &= (-i\omega_a - \kappa_a)a(t) - 2\pi |g|^2 \int_0^t a(\tau) e^{(-i\omega_a - \kappa_m)(t-\tau)} \sum_{l=-\infty}^{\infty} (-1)^{l(N-1)} \delta[\Delta\omega(t-\tau - l\frac{2\pi}{\Delta\omega})] d\tau \\ &= (-i\omega_a - \kappa_a)a(t) - \frac{\pi |g|^2}{\Delta\omega} a(t) - \sum_{l \neq 0} (-1)^{l(N-1)} \frac{2\pi |g|^2}{\Delta\omega} a(t - l\frac{2\pi}{\Delta\omega}) e^{(-i\omega_a - \kappa_m)(t-\tau)}. \end{aligned} \quad (\text{S37})$$

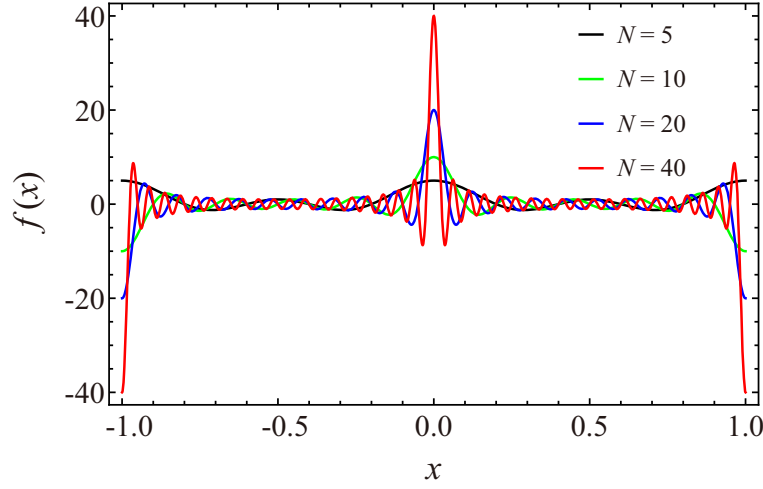


FIG. S1: The plot of the function $f(x) = \frac{\sin[\frac{N}{2}x]}{\sin[\frac{1}{2}x]}$.

For $t < \frac{2\pi}{\Delta\omega}$, the cavity photon experiences single exponential decay

$$\frac{d}{dt}a(t) = (-i\omega_a - \kappa_a)a(t) - \frac{\pi|g|^2}{\Delta\omega}a(t), \quad (\text{S38})$$

with solution

$$a(t) = a(0)e^{-(i\omega_a + \kappa_a + \frac{\pi|g|^2}{\Delta\omega})t}. \quad (\text{S39})$$

We can see that the cavity photon decay is enhanced by $\frac{\pi|g|^2}{\Delta\omega}$.

For $\frac{2\pi}{\Delta\omega} \leq t \leq 2\frac{2\pi}{\Delta\omega}$, we have

$$\frac{d}{dt}a(t) = (-i\omega_a - \kappa_a - \frac{\pi|g|^2}{\Delta\omega})a(t) + \frac{2\pi|g|^2}{\Delta\omega}a(t - \frac{2\pi}{\Delta\omega})e^{-(i\omega_a - \kappa_m)\frac{2\pi}{\Delta\omega}}, \quad (\text{S40})$$

$$= (-i\omega_a - \kappa_a - \frac{\pi|g|^2}{\Delta\omega})a(t) + \frac{2\pi|g|^2}{\Delta\omega}a(0)e^{-(i\omega_a - \kappa_m)\frac{2\pi}{\Delta\omega}}e^{-(i\omega_a + \kappa_a + \frac{\pi|g|^2}{\Delta\omega})(t - \frac{2\pi}{\Delta\omega})}. \quad (\text{S41})$$

Therefore, the cavity photons show a revival due to the energy of magnons coupling back to the cavity

$$a(t) = -\frac{2\pi|g|^2}{\Delta\omega}a(0)e^{-(i\omega_a - \kappa_m)\frac{2\pi}{\Delta\omega}}(t - \frac{2\pi}{\Delta\omega})e^{-(i\omega_a + \kappa_a + \frac{\pi|g|^2}{\Delta\omega})(t - \frac{2\pi}{\Delta\omega})}. \quad (\text{S42})$$

D. Scattering Picture

Above, we have adopted a direct solution of the temporal equations of motion. Alternatively, one can also discuss the MGM as a scattering problem in frequency space. We employ the equations of motion, Eqs. (S10) and (S11), supplement them with the input field (as in Eq. (S4)), and obtain, in frequency space:

$$-i\omega a = (-i\omega_a - \kappa_a)a - i \sum_j g_j m_j - i\sqrt{2\kappa_{a,1}}E_{\text{in}} \quad (\text{S43})$$

$$-i\omega m_j = (-i\omega_j - \kappa_m)m_j - ig_j^* a. \quad (\text{S44})$$

Here the functions a , m_j , and E_{in} are understood to be functions of the frequency ω .

These equations can be solved by eliminating m_j in favor of a and then applying the input-output relation Eq. (S5). This leads to the following result for the frequency-dependent reflection amplitude that gives $E_{\text{out}}(\omega) = r(\omega)E_{\text{in}}(\omega)$:

$$r(\omega) = \frac{[\omega_a - \omega + \Sigma(\omega)] + i(\kappa_{a,1} - \kappa_{a,0})}{-[\omega_a - \omega + \Sigma(\omega)] + i(\kappa_{a,1} + \kappa_{a,0})}. \quad (\text{S45})$$

At this point we have introduced the “MGM self-energy” that describes the collective effects of all the magnon modes acting on the cavity mode:

$$\Sigma(\omega) = \sum_j \frac{|g_j|^2}{\omega - \omega_j + i\kappa_m}. \quad (\text{S46})$$

The real part of Σ describes the effective frequency shift, while the imaginary part describes additional damping (induced by the magnon mode damping). The reflection amplitude can be decomposed into magnitude and phase shift:

$$r(\omega) = |r(\omega)|e^{i\theta(\omega)}. \quad (\text{S47})$$

In the ideal case without intrinsic losses ($\kappa_{a,0} = \kappa_m = 0$), we have $|r| = 1$. The time-delay of a scattered wave-packet is determined by the derivative of the phase shift with respect to frequency:

$$\tau(\omega) = \frac{\partial\theta(\omega)}{\partial\omega}. \quad (\text{S48})$$

The most important necessary condition for a useful memory is that this time-delay be constant over the bandwidth interval $N\Delta\omega$, i.e. the slope of θ should be constant. In the limit of small magnon-cavity coupling $g \rightarrow 0$ (and no intrinsic losses), each magnon resonance leads to a step of 2π in the phase shift θ . A finite g rounds off these steps. In the vicinity of each resonance, we can then approximate $\Sigma \approx g^2/(\omega - \omega_j)$, which leads to a phase shift rising like $\theta(\omega) - \theta(\omega_j) = 2\kappa_{a,1}(\omega - \omega_j)/g^2$. In order to have a constant overall slope of θ , we have to match this to the slope $T = 2\pi/\Delta\omega$ that is dictated by the spacing of resonances and which corresponds to the ideal storage time. That leads to the critical coupling condition (without intrinsic losses)

$$\frac{\pi g^2}{\Delta\omega} = \kappa_{a,1}. \quad (\text{S49})$$

We note that this condition remains true (in the present form) if intrinsic cavity losses are also incorporated, i.e. when $\kappa_{a,0} \neq 0$. The contribution from $\kappa_{a,0}$ cancels when deriving the condition. We note, however, that for finite $\kappa_{a,0}$ this condition slightly differs from the critical coupling condition derived below from demanding zero reflection of the input pulse. This is because, in general, for finite $\kappa_{a,0}$, the form of the critical coupling condition depends on the precise physical condition that is imposed. Still, one needs ideally $\kappa_{a,0} \ll \kappa_{a,1}$ to suppress unwanted losses and to avoid a resonance structure showing up in the magnitude $|r|$ of the reflection. In addition, the cavity mode acts like a filter, which should be broad enough to cover the whole magnon spectrum, i.e.

$$\kappa_{a,1} \gg N\Delta\omega. \quad (\text{S50})$$

Taking these two conditions together also implies $g \gg \kappa_{a,1}/\sqrt{N}$, as stated already in Eq. (S28). In addition, to keep the magnon losses small (ensuring $|r|$ close to 1), one needs $\kappa_m \ll \Delta\omega/2\pi$, as stated in Eq. (S26).

E. Critical coupling condition

From Eq. (S39), the microwave pulse input into the cavity couples to the external coupling channel (rate $\kappa_{a,1}$) and the temporal bright mode ($\frac{\pi|g_0|^2}{\Delta\omega}$), and also dissipates ($\kappa_{a,0}$) due to intrinsic radiation and absorption losses. Therefore, the full internal loss of the cavity is actually $\kappa'_{a,0} = \kappa_{a,0} + \frac{\pi|g_0|^2}{\Delta\omega}$. To suppress the reflection of the input pulse, the critical coupling (impedance matching) condition $\kappa_{a,1} = \kappa'_{a,0} = \kappa_{a,0} + \frac{\pi|g_0|^2}{\Delta\omega}$ is desired. The storage and retrieval efficiency of the MGM can be greatly affected by the critical coupling condition of the MGM with the coaxial

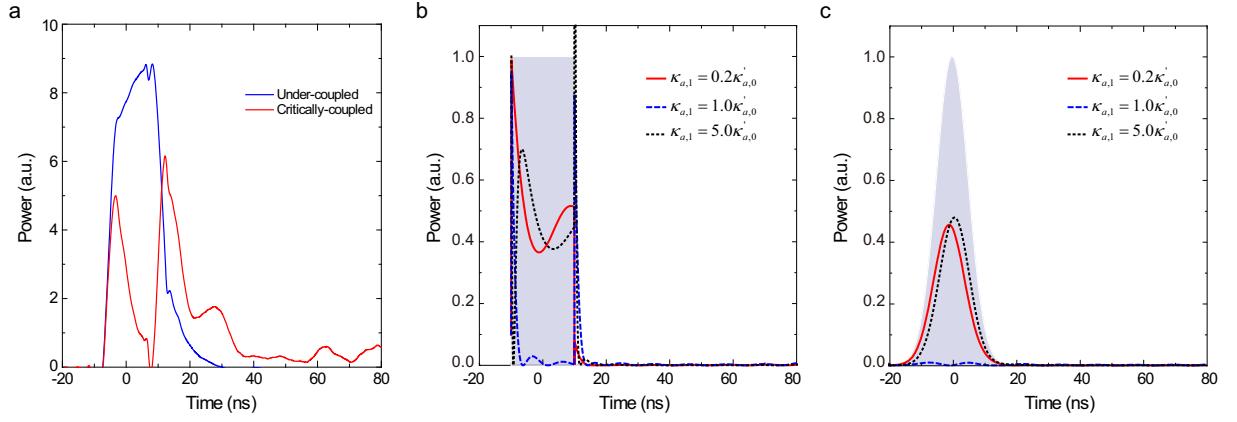


FIG. S2: Input reflection at various coupling conditions. a, Measured input reflections for microwave pulses to the microwave cavity with under-coupled ($\kappa_{a,1} < \kappa'_{a,0}$, blue curve) and critically coupled ($\kappa_{a,1} \approx \kappa'_{a,0}$, red curve) probes, respectively. b, The calculated cavity reflection for a rectangular pulse input (shadow region) at various coupling conditions. c, The calculated cavity reflection for a Gaussian input pulse using the same parameters as in b.

probe. If the MGM is under-coupled, a large portion of the energy will be reflected as the signal gets in and out of the cavity, and as a result the MGM efficiency becomes low.

In our measurements, we did observe a strong reflection peak at the time of input for the undercoupling situation, and such reflection peak can be eliminated after adjusting the external coupling rate to meet the critical coupling condition, as plotted in Fig. S2a. Such an observation agrees well with the theoretical predication (Fig. S2b). Note that there is still some residual reflection for the critical coupling condition, which is attributed to the step response of the MGM to the rectangular input pulse (both the rising and falling edges). This imperfection can be suppressed by choosing Gaussian pulse inputs (Fig. S2c).

F. Photon Retrieval

From Eq. (S42), after one period $T = \frac{2\pi}{\Delta\omega}$ the stored energy will couple back to the cavity, which leads to the retrieval of the photons. We can solve for the detected microwave amplitude by the input-output formula Eq. (S5), with the input microwave also taken into account. Substituting the experiment parameters into the equation of the cavity field, with the input rectangular pulse duration $t_p = 20$ ns, we obtained the dynamics in Fig. S3a. The analytical and numerical results agree well with each other. With the given parameters, the numerical solution shows a memory efficiency of $\zeta = 0.33$, which is the integrated total output energy in the first retrieval peak as compared with that of the input pulse.

From the asymptotic solution, we can derive the efficiency of the magnon gradient memory as

$$\zeta \approx e^{-2\kappa_m \frac{2\pi}{\Delta\omega}} \left[1 - \frac{1}{t_p \left(\kappa_{a,0} + \frac{\pi|g|^2}{\Delta\omega} \right)} \right] \left(\frac{\frac{\pi|g|^2}{\Delta\omega}}{\kappa_{a,0} + \frac{\pi|g|^2}{\Delta\omega}} \right)^2 \quad (\text{S51})$$

for a rectangular input pulse under critical coupling condition (which demands zero reflection). Note that the pulse duration is limited by the external coupling rate: $t_p > 1/\kappa_{a,1} = 1/(\kappa_{a,0} + \frac{\pi|g|^2}{\Delta\omega})$.

In Fig. S3b, we plot the efficiency as a function of the coupling strength g_0 . A comparison of the numerical results with the asymptotic solutions shows that they agree well with each other for $g/2\pi \geq 7$ MHz. The efficiency saturates to $\zeta = e^{-2\kappa_m \frac{2\pi}{\Delta\omega}} \approx 0.403$ for $\frac{\pi|g_0|^2}{\Delta\omega} \gg \kappa_{a,0}$, which is limited by the intrinsic loss of the magnon. Figure S3c plots the behavior of the memory for various coupling strengths, which shows the saturated retrieval peak at 100 ns. If we can reduce the magnon dissipation rate, as shown in Fig. S3d, the retrieval efficiency approaches unity. If operating at low temperatures, the magnon linewidth can be reduced to 0.042 MHz [S3], which will lead to a saturated efficiency of 0.95 for a storage time $\frac{2\pi}{\Delta\omega} = 100$ ns.

[S3] Spencer, E. G., LeCraw, R. C., and Linares, R. C., Jr. *Phys. Rev.* **123**, 1937 (1961)

By numerical calculation, we further studied the memory for different input pulse detuning and frequency gradient of the magnons. From our analytical solutions, we can expect the effective bandwidth of the MGM to be about $\kappa'_{a,0} = \kappa_{a,0} + \frac{\pi|g_0|^2}{\Delta\omega} \approx \frac{\pi|g_0|^2}{\Delta\omega}$ for $N \rightarrow \infty$. However, in experiments we have a finite N , and therefore the bandwidth is also limited by the bandwidth of the gradient magnon spectrum, which is about $N\Delta\omega$. Therefore, the highly efficient memory works in a bandwidth of $\min\{\frac{\pi|g_0|^2}{\Delta\omega}, N\Delta\omega\}$. From Fig. S4a, the bandwidth is about $8\Delta\omega$, which is consistent with our theory. Figure S4b shows that the storage time is inversely proportional to $\Delta\omega$, which also agrees with our expectation.

G. Measurement Scheme

Figure S5a illustrates the device schematic of the MGM with eight YIG spheres. Note that the radius (3 mm) of the small coils is much larger than the YIG sphere radius to ensure the magnetic fields generated by the coils are uniform at the position of the YIG sphere (1 mm above the coil). As a result, the coils have to be placed 6.5 mm apart from one another, and so are the YIG spheres. Since the magnetic field of the cavity TE_{110} mode has a cosine distribution along the \vec{x} direction inside the cavity (Figs. S5b & c), different YIG spheres experience different magnetic field strengths. Therefore the coupling strength of the magnon modes with the cavity mode are not identical, and this contributes to the non-ideality of the MGM. Such non-ideality is unavoidable, but in our experiment efforts such as placing the YIG spheres as close to the center as possible have been taken to reduce the non-ideality in the device.

There are three types of measurement involved in our experiments.

(1) First is the *cavity reflection spectrum measurement*. The input signal is provided and the reflected signal is detected by a vector network analyzer, as indicated in Fig. S6a. A circulator is used to separate the input and reflected signals to avoid undesired interference.

(2) The second type of measurement is the *time trace measurement*, which is carried out using a high-speed oscilloscope (Fig. S6b). The signal from a microwave source is modulated by a pulse generator through a transistor-transistor logic (TTL) switch to obtain a pulsed microwave signal, which is sent into the device, and then a retrieval pulse can be measured after the pre-programmed retrieval time.

(3) The third type of measurement is the *coherence measurement*, as shown in Fig. S6c. The scheme is similar to the time trace measurement but with an interferometer added. The input signal is split into two branches, one of which is used as the reference to interfere with the output signal. The setup is very similar to the Mach-Zehnder interferometer commonly used in optical measurements. By varying the phase of the reference, the amplitude of the interference signal changes, and their relation is measured to characterize the retrieval pulse coherence.

H. Experimental Imperfections

The operation of the MGM requires the hybrid magnon-photon modes evenly distributed in the frequency domain, which will give a perfect constructive interference at the pre-programmed retrieval time T , and best suppression of the fringes at other times. Imperfection in the frequency distribution will result in deteriorated signal re-construction. This is clearly illustrated by the comparison given in Fig. S7. For a uniformly distributed spectrum, the retrieval pulse is very clean; while for the non-uniformly distributed spectrum, the retrieval pulse is severely distorted.

In our experiments, we can precisely tune the small coil to obtain a near perfect gradient for the magnon modes. The small experimental imperfections only have very slight effects on the performance of the MGM. To investigate the influence of the experimental imperfection on the efficiency of the MGM, we simulated the efficiencies for various parameters, with random perturbations to the ideal case, where

$$g_j = g_0 \times (1 + \xi_j), \quad (\text{S52})$$

$$\omega_j = \omega_a + (j - \frac{N-1}{2})\Delta\omega_m + \Delta\omega_m \times \xi_j. \quad (\text{S53})$$

Here, $\xi_j \in [-0.1, 0.1]$ is a uniformly distributed random variable, which means the variations of magnon frequency and coupling strengths are within a range of $\pm 10\%$.

The results for 500 sets of different parameters are shown in Fig. S8, with the mean value of ζ being about 0.30, while the standard deviation is 0.009. For such a high imperfection up to 10%, the MGM still shows a very good ability for signal re-construction. Therefore, the performance of the MGM is very robust against experimental imperfections.

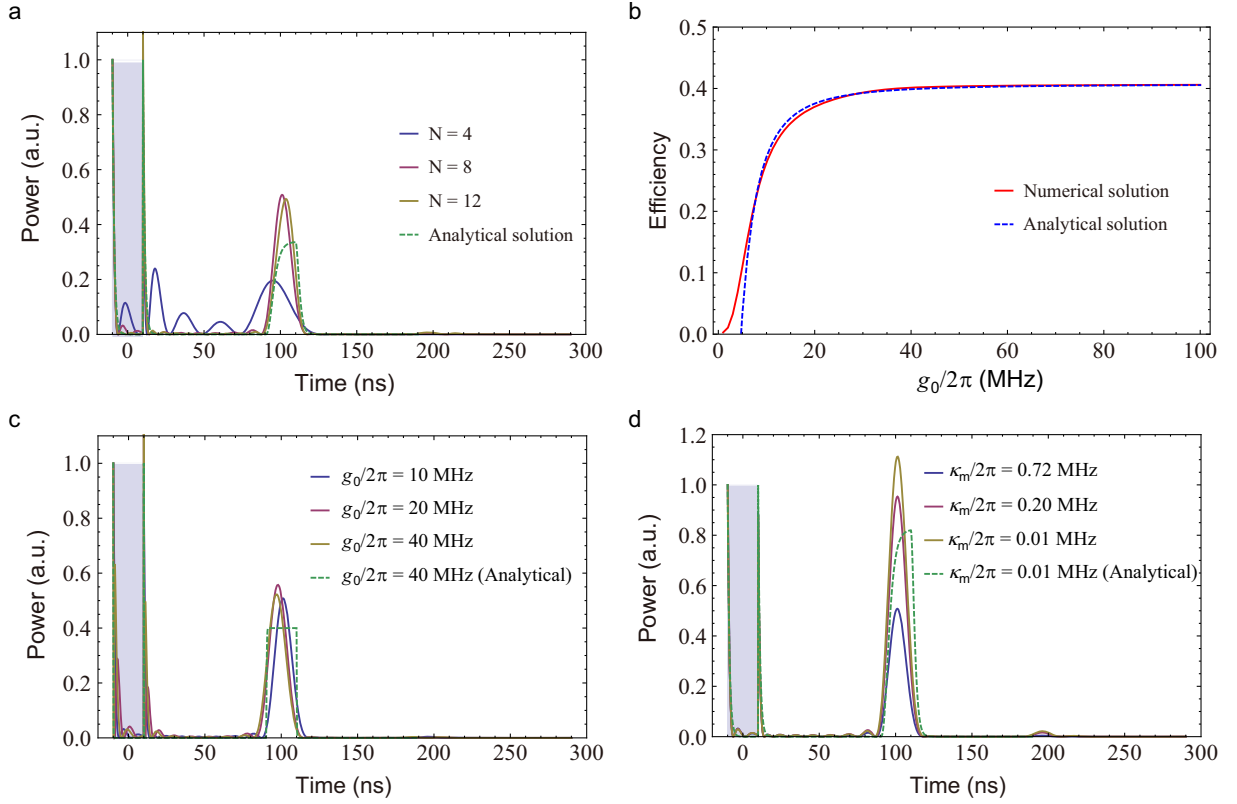


FIG. S3: a, Calculated dynamics of the MGMs with different YIG sphere numbers (N). b, Comparison of the numerical and analytical solutions at various coupling strengths. c & d, dynamics of the MGM with various coupling strengths and magnon dissipation rates, respectively. For each plot, the solid and dashed curves represent the numerical and analytical solutions, respectively. All parameters (beside the varying parameters) are taken from the experiments: $N_s = 8$, $g_0 = 2\pi \times 10$ MHz, $\Delta\omega = 2\pi \times 10$ MHz, $\kappa_{a,0} = 2\pi \times 3$ MHz, $\kappa_m = 2\pi \times 0.72$ MHz, $\kappa_{a,1} = \kappa_{a,0} + \frac{\pi|g_0|^2}{\Delta\omega}$ (critical coupling), and the input pulse duration is $t_p = 20$ ns.

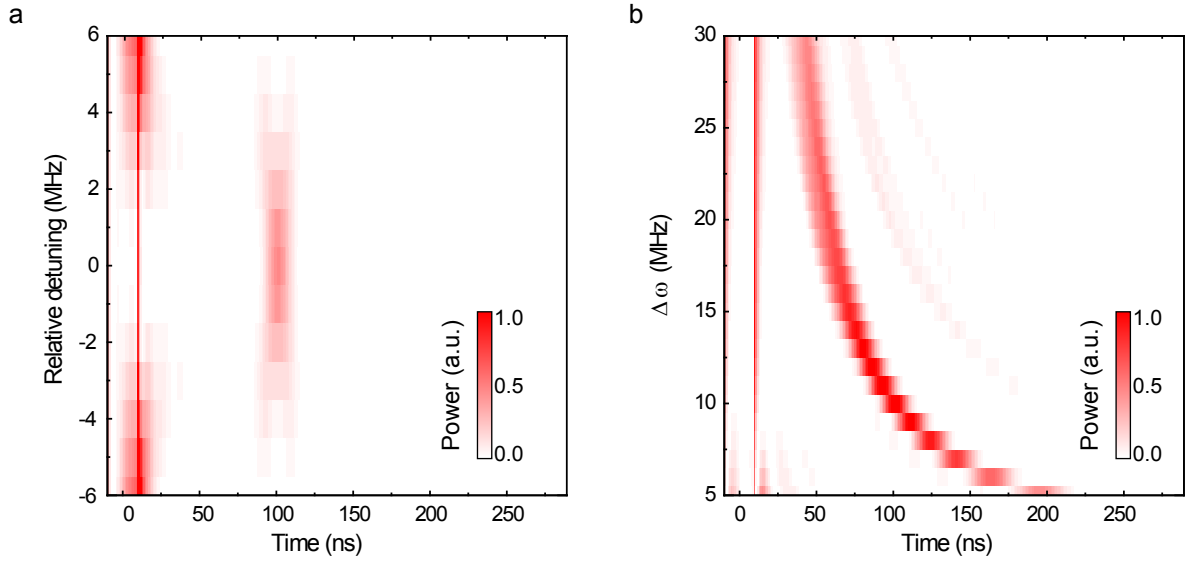


FIG. S4: The calculated reflection signal dynamics at (a): various input microwave detunings $(\omega_{in} - \omega_a)/\Delta\omega$, and (b): various magnon frequency gradients $\Delta\omega$. In the calculation, we assume all the magnon modes are identical, have uniform coupling strength, and are evenly distributed. Other parameters are from our experiment: $N_s = 8$, $g_0 = 2\pi \times 10$ MHz, $\Delta\omega = 2\pi \times 10$ MHz, $\kappa_{a,0} = 2\pi \times 3$ MHz, $\kappa_m = 2\pi \times 0.72$ MHz, $\kappa_{a,1} = \kappa_{a,0} + \frac{\pi|g_0|^2}{\Delta\omega}$ (critical coupling) and the input pulse duration is $t_p = 20$ ns.

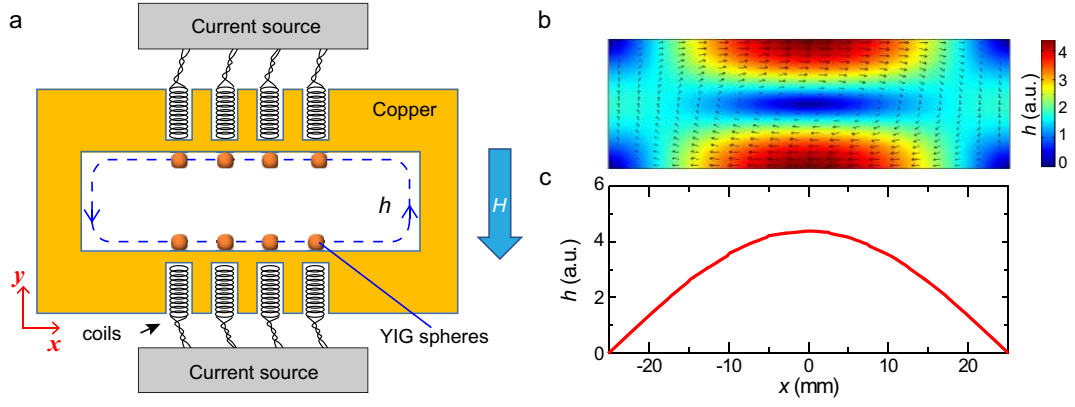


FIG. S5: a, Device schematic of the MGM consisting of eight YIG spheres. b, The intensity and direction of magnetic field distribution of the cavity TE₁₁₀ mode. Only the xy cross-section is shown because the magnetic field of this mode is almost uniform along the z direction. c, The cosine function-like magnetic field distribution along the x direction on the cavity wall where the YIG spheres are located.

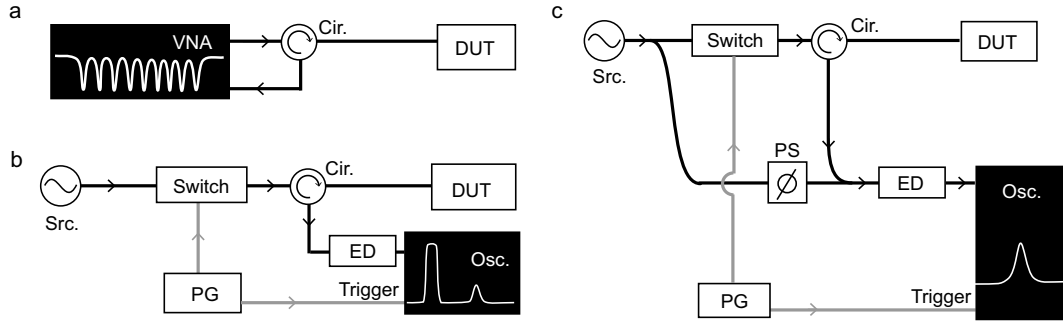


FIG. S6: Schematic of the measurement setup for the frequency spectrum of the cavity reflection (a), the time trace after a pulse excitation (b), and the coherence of the retrieved pulse (c), respectively. VNA: vector network analyzer; DUT: device-under-test; Cir.: circulator; Src.: microwave source; ED: envelop detector; PG: pulse generator; Osc.: oscilloscope; PS: phase shifter.

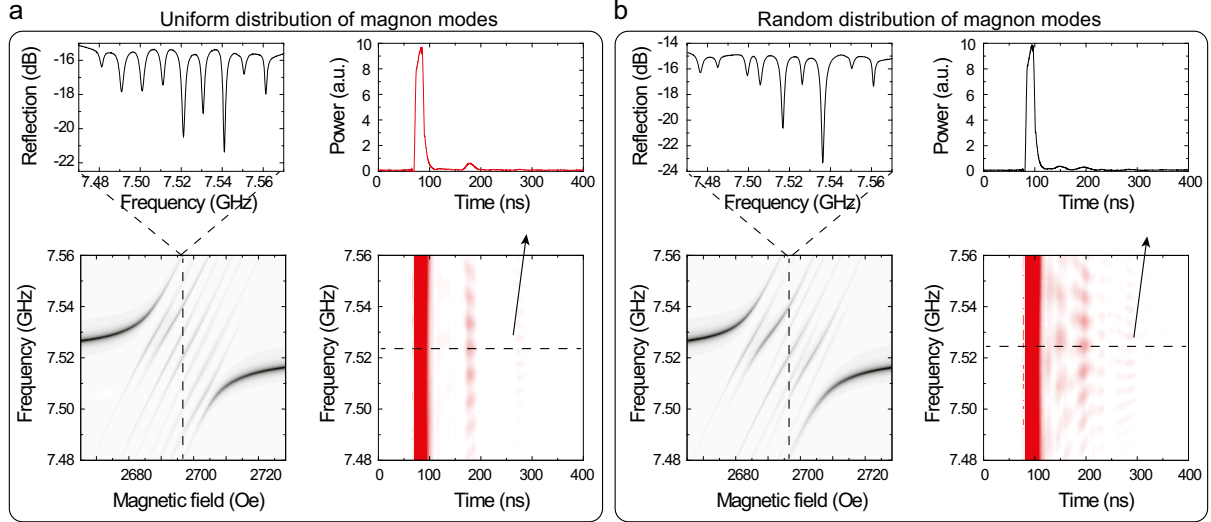


FIG. S7: Comparison of the frequency spectrum and time trace for the uniformly (a) and randomly (b) distributed magnon mode scenarios, respectively. In each panel, the left side is the frequency spectrum and the right side is the time trace; the bottom rows are the results at different bias magnetic fields, while the top rows are the specific cases indicated by the dashed lines in the bottom rows.

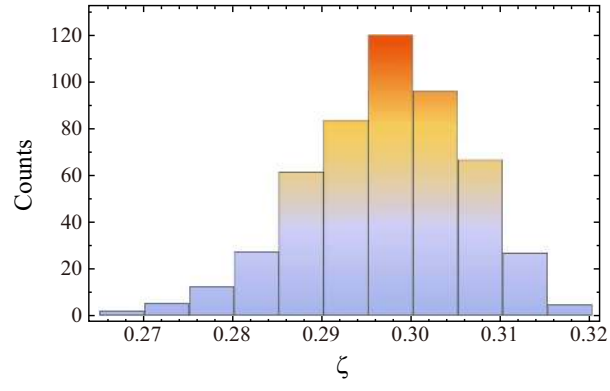


FIG. S8: The statistics of the numerically solved memory efficiency for randomly varied parameters g_j and ω_j .